Silicon Micro-Ring Modulator Modeling

Yoojin Ban

The Graduate School

Yonsei University

Department of Electrical and Electronic Engineering

Silicon Micro-Ring Modulator Modeling

A Master Thesis

Submitted to the Department of Electrical and Electronic Engineering

and the Graduate School of Yonsei University

in partial fulfillment of the

requirements for the degree of

Master of Electrical and Electronic Engineering

Yoojin Ban

February 2015

This certifies that the master's thesis of Yoojin Ban is approved.

_____

Thesis Supervisor: Woo-Young Choi

_____

Sang-Kook Han

_____

Myung-Jae Lee

The Graduate School

Yonsei University

February 2015

CONTENTS

CHAPTER

LIST OF FIGURES

LIST OF TABLES

ABSTRACT

Silicon Micro-Ring Modulator Modeling

By

Yoojin Ban

Department of Electrical and Electronic Engineering

The Graduate School

Yonsei University

A model for Si micro-ring modulator (Si MRM) is developed. Si MRM provides higher bandwidth and more energy-efficient solutions to many interconnect applications in a cost-effective manner with photonics or electronics alone.

Our model is derived from the coupled-mode theory and has the well-known second-order system characteristics with two complex poles and one real negative zero. For successful realization of EPICs, We implement simple and easy-to-use model to co-simulate Si MRM and electronic circuits on a single simulation platform in the initial design stage. Specifically, we develop a behavioral model for photonic devices and implement it in Verilog-A.

The model provides very accurate description of Si micro-ring modulator modulation characteristics and allows intuitive interpretation based on the pole-zero diagram. The accuracy of our model is compared with other previously reported small-signal models as well as measurement results. Using our model, the conditions for the best modulation efficiency can be determined and the large-signal transient characteristics can be explained with key device parameters. For the verification of our model, we compared the measured and simulated DC transmission characteristics, AC characteristics, and step-response as well as eye-diagram of the Si MRM. The simulation results based on our behavioral model shows fairly good agreements with the measurements.

***Keywords**:* Coupled mode analysis, electro-optic modulation, micro-ring modulators, silicon photonics.

1. Introduction

Electrical interconnects based on copper traces and wires has largely dominated interconnection applications over the past few decades, however, now they are struggling to handle continuously increasing data rates attributable to the remarkable advances in semiconductor technology and acceleration in microprocessor performance. Therefore, need for new technological solution that can supply high-data rate is begin to arise to solve the problems that existing electrical interconnects face such as short-reach length as well as power consumption, channel crosstalk, and electromagnetic interference [1], [2]. Optical interconnects technology is the one such technology mitigating these challenges associated with electrical interconnects. However, optical interconnects have largely been used to transmit over long distances as yet, and significant challenges remain such as low-cost and compact solution. Figure 1-1 shows current status of optical and electrical interconnects system as a function of transmission distance.

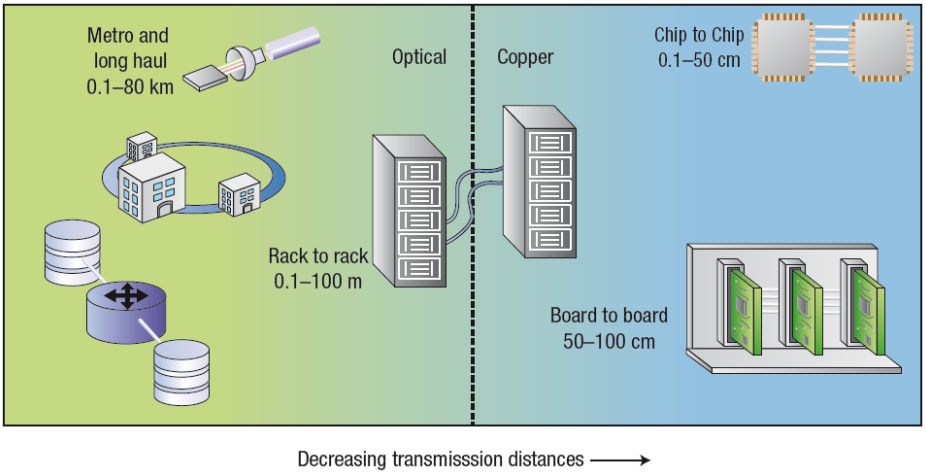

Fig 1-1. The market adoption of communication technology (optical versus electrical) as a function of transmission distance.

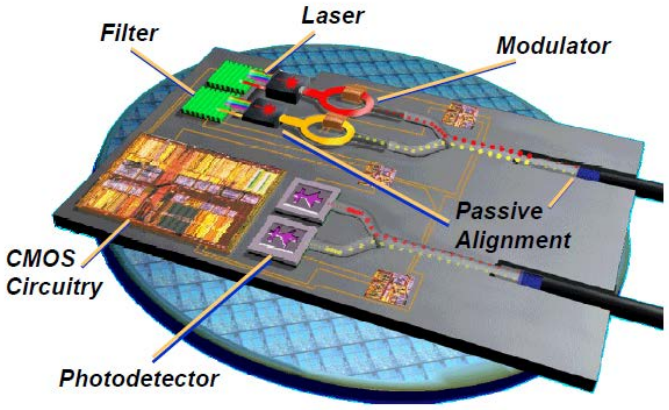

Fig 1-2. Conceptual diagram of full integration on a Si photonic chip.

Si photonics is attracting an explosive amount of research and development efforts ranging from rack-to-rack, board-to-board, and chip-to-chip optical interconnects. Its pronouncing breakout is mainly based on reusing the same complementary metal-oxide-semiconductor (CMOS) fabrication infrastructures and development of practical SOI-based photonic ICs that enable cost-effective, high-bandwidth, and small-footprint optical interconnect systems [3], [4]. These advantages will be maximized with development of monolithic electronic-photonic integrated circuits (EPICs) based on CMOS or bipolar CMOS (BiCMOS) technology [5], [6]. Figure 1-2 shows a conceptual diagram of full integration on Si photonic chip.

Among several photonic devices that can be used for Si photonic interconnect system realization, Si electro-optic (EO) modulator is one of the key components. In particular, Si micro-ring modulators (Si MRMs) are heavily investigated which can provide large bandwidth and high modulation efficiency with a small size and low power consumption [7]–[9]. In designing Si MRMs for optical interconnect applications, having an accurate and easy-to-use model for its modulation characteristics is very important especially for co-simulation with electronic circuits, modulator driver electronics, using standard electronic design automation (EDA) tools.

In this thesis, therefore, numerical and analytical models of Si MRM dynamics based on the physical structure are introduced. There are two

different approaches to obtain the models. Method of parameter extraction of the key parameters of the model with measurement is presented and the models are verified with AC responses and transit responses. Optimal operation conditions for Si MRMs are also introduced.

TABLE I

COMPARISON BETWEEN DIFFERENT TYPES OF MODULATORS

Modulators	ADVANTAGES	Challenges
Si MZM	Easy tuning (coarse, small range)	Inefficient, large size, high power consumption
Ring/disk	Very small and efficient	Dynamic fine tuning over large range
Hybrid EAM	Very short, very efficient	Optical loss ~10 dB, complicated fabrication
Other materials	Very short and efficient, no tuning issues	Immature fabrication development

2. Si MRM in Si Photonics

In Si EO modulators in Fig. 2-1, free-carrier plasma dispersion effect, modulation is the most commonly used method to convert input electrical signal to output optical signal. More specific, electrical signal applied on metal-oxide-semiconductor (MOS) capacitors, P-I-N junction or P-N junction implemented waveguide manipulates free-carrier concentration in waveguide and cause change of refractive index [10].

There are two types of EO modulators: Si Mach-Zehnder modulators (MZMs) and Si MRMs. Si MZMs are based on optical interferometer structures and have advantages of stable operation. However, their footprint becomes too big to ignore in high-data rate. Si MRMs are based on optical micro-ring resonator structure and enable to reduce foot print dramatically. Moreover, they owe low power consumption to their small foot print. We concentrate on the Si MRM consists of Si MRR with implemented P-N junction based optical phase shifter in this thesis which provide large bandwidth and high modulation efficiency with a small size and low power consumption.

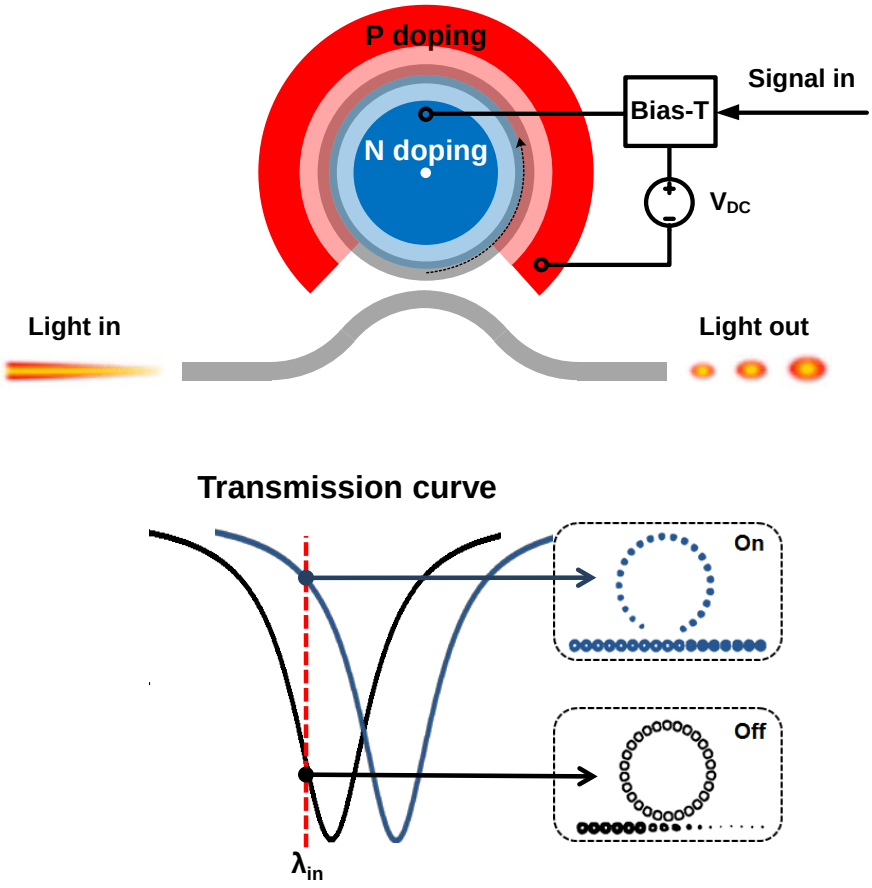

Fig 2-1. Conceptual operation principle of Si MRM.

2-1. Optical Micro-Ring Resonator

2-1-1. Multiple Round-Trip Approach

Figure 2-2(a) shows the structure of the MRR used for our investigation which consists of one straight bus waveguide and one ring waveguide. Input light passing through the bus waveguide is partially coupled into the ring waveguide and experiences phase shifts and losses as it circulates the ring waveguide. A portion of the circulating light couples out of the ring into the bus waveguide, and experiences interference. These interactions can be described using matrix formation as

$$\begin{pmatrix} E_o \\ E'_o \end{pmatrix} = \begin{pmatrix} \gamma & -j\kappa \\ -j\kappa & \gamma \end{pmatrix} \begin{pmatrix} E_i \\ E'_i \end{pmatrix} \text{and} \qquad (2.1)$$

$$E'_i = \alpha \exp(-j\theta) E'_o, \qquad (2.2)$$

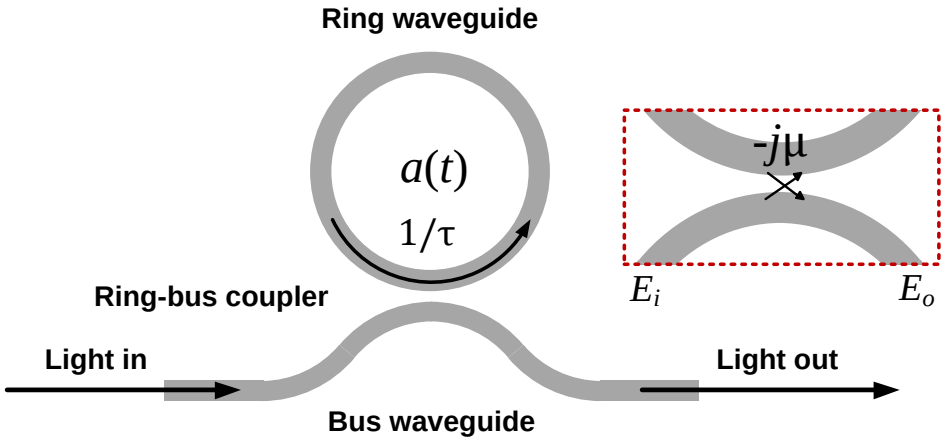

Fig 2-2(a). Micro-ring resonator structure for round-trip approach

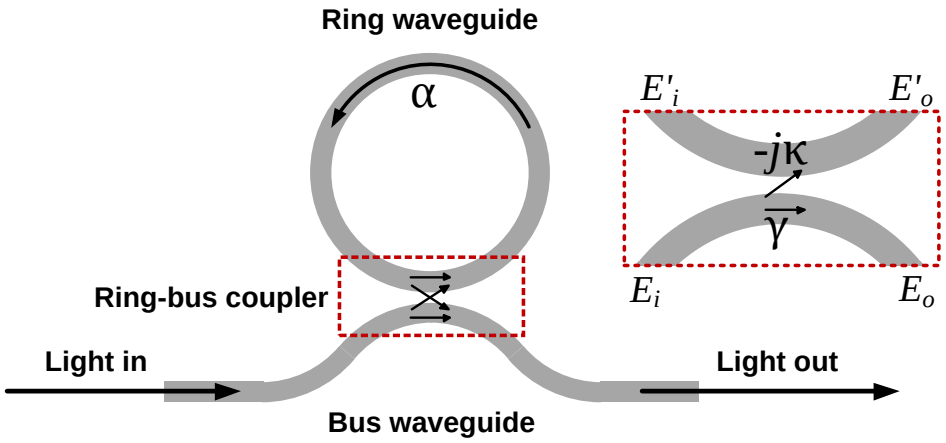

Fig 2-2(b). Micro-ring resonator structure for coupled-mode approach

where complex optical field amplitude E are normalized that square magnitude of E becomes power. As can be seen in the picture, E_i, E_o, E'_i, and E'_o are optical field amplitudes of each port of ring-bus coupler. γ and κ are the through and coupling coefficient of the ideal loss-less ring-bus coupler satisfying $\gamma^2 + \kappa^2 = 1$, and α is the round-trip loss coefficient of the ring waveguide. θ is round-trip phase shift satisfying $\theta = 2\pi\eta_0 L/\lambda$, where η_0 is the group refractive index for the ring waveguide, L is the round-trip length, and λ is wavelength of the input light in free-space.

Using the multiple round-trip approach [11], output optical field amplitude E_o becomes

$$\begin{aligned} E_o &= \left[\gamma - \kappa^2\alpha\exp(-j\theta) - \kappa^2\alpha^2\gamma\exp(-j2\theta) - \cdots\right]E^i \\ &= \left[\gamma - \kappa^2\sum_{n=1}^{\infty}\alpha^n\gamma^{n-1}\exp(-jn\theta)\right]E_i \\ &= \left[\gamma - \kappa^2\frac{\alpha\exp(-j\theta)}{1-\alpha\gamma\exp(-j\theta)}\right]E_i \\ &= \frac{\gamma - \alpha(\gamma^2+\kappa^2)\exp(-j\theta)}{1-\alpha\gamma\exp(-j\theta)}E_i \\ &= \frac{\gamma - \alpha\exp(-j\theta)}{1-\alpha\gamma\exp(-j\theta)}E_i, \end{aligned} \tag{2.3}$$

where n is nth round-trip. If the ring-bus coupler is lossy, transmission power level uniformly degraded and equation formula remains correct as long as

including coupler loss in to the round-trip loss coefficient α [12]. By squaring Eq. (2.3) transmission $T = P_o/P_i$ is expressed as

$$T = \frac{P_o}{P_i} = \frac{|E_o|^2}{|E_i|^2} = \frac{\alpha^2 + \gamma^2 - 2\alpha\gamma\cos(\theta)}{1 + \alpha^2\gamma^2 - 2\alpha\gamma\cos(\theta)}. \quad (2.4)$$

Lowest transmission occurs at on-resonance condition if θ is multiple of 2π and consequently L is multiple of the input wavelength in the ring waveguide λ/η_0. Mode number m at on-resonance condition can be expressed as

$$m = \frac{L}{\lambda_0 / \eta_0} = \frac{\eta_0 \omega_0 L}{c}, \quad (2.5)$$

where λ_0 is resonance wavelength in free-space, ω_0 is resonance angular frequency, and c is speed of light. Transmission at on-resonance becomes

$$T = \frac{\alpha^2 + \gamma^2 - 2\alpha\gamma}{1 + \alpha^2\gamma^2 - 2\alpha\gamma} = \frac{(\alpha - \gamma)^2}{(1 - \alpha\gamma)^2}. \quad (2.6)$$

If α is equal to γ, Eq. (2.6) becomes zero and this condition is called critical coupling. This condition means power loss in the ring (1- α^2) is equal to coupling power (κ^2). $\alpha < \gamma$ and $\alpha > \gamma$ conditions are called under- and over-coupling, respectively.

Using Eq. (2.4), we can obtain spectral characteristic of the MRR. Figure 2-2 shows wavelength-dependent transmission curve for 10-μm radius MRM with 4 η_0, 0.95 α, and 0.95 γ.

There are several parameters that can describe MRR. First one is the distance between resonance deeps called free spectral range (FSR) given as

$$\text{FSR} = \frac{\lambda^2}{\eta_0 L}. \tag{2.7}$$

Next one is Full width at half maximum (FWHM) of the transmission curve is given as

$$\text{FWHM} = \frac{(1-\alpha\gamma)\lambda_0^{\,2}}{\pi\eta_0 L\sqrt{\alpha\gamma}}. \tag{2.8}$$

The quality factor (Q-factor) means the sharpness of the resonance defined as

$$\text{Q-factor} = \frac{\lambda_0}{\text{FWHM}} = \frac{\pi\eta_0 L\sqrt{\alpha\gamma}}{(1-\alpha\gamma)\lambda_0}. \tag{2.9}$$

Higher Q-factor is obtained by large L and low loss in resonator, however, these two factors are not independent since larger L produces higher

accumulated propagation round-trip loss [12].

2-1-2. Coupled-Mode Approach

Coupled-mode approach is a perturbation analysis method that is often used to describe systems having coupled resonator modes with simple equations [13]. Using coupled-mode equations, we can simplify ring dynamics by viewing MRR as a small lumped oscillator of normalized energy amplitude $a(t)$ that $|a(t)|^2$ is defined as the total energy stored in the ring waveguide at time t. Stored energy has relationship with power flowing through the ring waveguide. Flowing optical field amplitude in ring waveguide $A(t)$ is normalized to satisfy that $|A(t)|^2$ represents the total power flowing through any cross section of the ring waveguide. The relationship between $|a(t)|^2$ and $|A(t)|^2$ is

$$\left|a(t)\right|^2 = \left|A(t)\right|^2 \frac{\eta_0 L}{c} = \left|A(t)\right|^2 \frac{\eta_0 L}{T}, \qquad (2.10)$$

where T is round-trip time of the ring waveguide.

With the coupled-mode equations, MRR dynamics can be described as [14]

$$\frac{da(t)}{dt} = \left(j\omega_0 - \frac{1}{\tau} \right) a(t) - j\mu E_i(t) \text{ and} \qquad (2.11)$$

$$E_o(t) = E_i(t) - j\mu a(t). \qquad (2.12)$$

Using Eq. (2.5) ω_0, the resonance angular frequency of the MRR is expressed as

$$\omega_0 = \frac{2\pi mc}{\eta_0 L}. \tag{2.13}$$

τ is a decay time constant satisfying

$$\frac{1}{\tau} = \frac{1}{\tau_l} + \frac{1}{\tau_e}, \tag{2.14}$$

where τ_l and τ_e are decay time constants due to the round-trip loss and ring-bus coupling, respectively. They are related to α and γ which are parameters used in multiple round-trip approach in the following manner;

$$\tau_l = \frac{2\eta_0 L}{(1-\alpha^2)c} \text{ and} \tag{2.15}$$

$$\tau_e = \frac{2\eta_0 L}{(1-\gamma^2)c}. \tag{2.16}$$

μ is the mutual coupling coefficient satisfying

$$\mu^2 = \frac{\kappa^2}{T} = \frac{2}{\tau_e}. \tag{2.17}$$

Parameters described above are depicted in Fig. 2-3 with MRR structure.

Suppose that E_i is given as $E_0\exp(j\omega t)$ where ω is the angular frequency of input light. General solution of Eq. (2.11) is the superposition of the homogeneous solution and the steady-state response as

$$a(t) = P\exp\left(j\omega_0 t - \frac{1}{\tau}t \right) + Q\exp(j\omega t), \tag{2.18}$$

where P and Q are arbitrary constants. Substituting Eq. (2.18) into Eq. (2.11), we have the identity

$$\begin{aligned} &P\left(j\omega_0 t - \frac{1}{\tau}t \right)\exp\left(j\omega_0 t - \frac{1}{\tau}t \right) + Q(j\omega)\exp(j\omega t) = \\ &P\left(j\omega_0 - \frac{1}{\tau} \right)\exp\left(j\omega_0 t - \frac{1}{\tau}t \right) + \left[Q\left(j\omega_0 - \frac{1}{\tau} \right) - j\mu E_0 \right]\exp(j\omega t). \end{aligned} \tag{2.19}$$

If t approaches infinity, only steady-state solution remains and we can obtain Q as

$$Q = \frac{-j\mu E_0}{j\omega - j\omega_0 + \frac{1}{\tau}}. \tag{2.20}$$

P is determined with initial condition of $a(t = 0)$. Steady-state solution of a(t) is

$$a(t) = \frac{-j\mu E_i}{j\omega - j\omega_0 + \frac{1}{\tau}}. \tag{2.21}$$

After substituting Eq. (2.21) into Eq. (2.12), we have

$$\begin{aligned} E_o &= \frac{j\omega - j\omega_0 + \frac{1}{\tau} - \mu^2}{j\omega - j\omega_0 + \frac{1}{\tau}} E_i \\ &= \frac{j\omega - j\omega_0 + \frac{1}{\tau_l} - \frac{1}{\tau_e}}{j\omega - j\omega_0 + \frac{1}{\tau}} E_i \end{aligned} \tag{2.21}$$

By squaring Eq. (2.21) transmission $T = P_o/P_i$ is expressed as

$$T = \frac{P_o}{P_i} = \frac{|E_o|^2}{|E_i|^2} = \frac{(\omega - \omega_0)^2 + \left(\frac{1}{\tau_l} - \frac{1}{\tau_e}\right)^2}{(\omega - \omega_0)^2 + \frac{1}{\tau^2}}. \tag{2.22}$$

Lowest transmission occurs at on-resonance condition, $\omega = \omega_0$ and transmission at on-resonance becomes

$$T = \frac{\left(\frac{1}{\tau_l} - \frac{1}{\tau_e}\right)^2}{\frac{1}{\tau^2}} = \frac{\left(\frac{1}{\tau_l} - \frac{1}{\tau_e}\right)^2}{\left(\frac{1}{\tau_l} + \frac{1}{\tau_e}\right)^2}. \qquad (2.23)$$

Critical coupling condition is that τ_l is equal to τ_e, and it is identical with the critical coupling condition from multiple round-trip approach that α is equal to γ. This condition means power loss in the ring is equal to powere loss in ring-bus coupler. $\tau_l < \tau_e$ and $\tau_l > \tau_e$ conditions are called under- and over-coupling, respectively.

Using Eq. (2.23), we can obtain spectral characteristic of the MRR. Figure 2-2 shows wavelength-dependent transmission curve with dotted line for 10-μm radius MRM with 4 η_0, 0.95 α, and 0.95 γ. Strip line represents transmission curve using multiple round-trip approach and these two lines are almost identical especially for low loss MRR.

FWHM of the transmission curve is given as

$$\text{FWHM} = \frac{\lambda_0^2}{\pi c \tau}. \qquad (2.24)$$

Q-factor is expressed as

$$\text{Q-factor} = \frac{\lambda_0}{\text{FWHM}} = \frac{\pi c \tau}{\lambda_0}. \tag{2.25}$$

Higher Q-factor is obtained by low loss in resonator.

2-2. Si Optical Phase Shifter

Applied electric field on a material may change real part ($\Delta\eta$) and imaginary part (Δk) of refractive index. Pockels effect, the Kerr effect and the Franz–Keldysh effect are electric field effects that are useful in semiconductor resulting in either electro-absorption which causes a change in Δk or electro-refraction which causes a change in $\Delta\eta$. However, these electric field effects are weak in silicon at the 1.55-μm wavelength [15]. Silicon has very large thermo-optic coefficient, however, it is too slow to achieve high-speed modulation [16].

Free-carrier plasma dispersion effect can be excellent alternative method to achieve high-speed modulation in silicon [10]. Concentration of free-carrier in silicon changes the real and imaginary parts of refractive index in silicon. At 1.55-μm wavelength, $\Delta\eta$ and Δk are experimentally produced as [17]

$$\Delta\eta = -5.4\times10^{-22}\Delta N^{1.011} - 1.53\times10^{-18}\Delta P^{0.838} \text{ and}$$
$$\Delta k = 8.88\times10^{-21}\Delta N^{1.167} + 5.84\times10^{-20}\Delta P^{1.109}, \qquad (2.26)$$

where ΔN and ΔP are changes of free-electron and fee-hole concentrations in silicon, respectively.

Electrical manipulation of the charge density interacting with the propagating light is achievable through mechanisms such as carrier injection, accumulation or depletion. Since depletion is suitable for high-speed operation, our interest is depletion type which can realized with reverse biased P-N junction.

3. Characteristics of Si MRM based on Reverse Biased PN-Junction

3-1. Device Description

Figure 3-1 shows the microphotograph and the cross-section structure, respectively, of a fabricated reverse-biased PN junction Si MRM used for verifying the accuracy our small-signal model. It is fabricated on 220-nm thick Si layer on 2-μm thick buried oxide (BOX) layer through the OpSIS-IME multi-project-wafer foundry service. Grating couplers having 127-μm pitch are used for optical I/O with a fiber array.

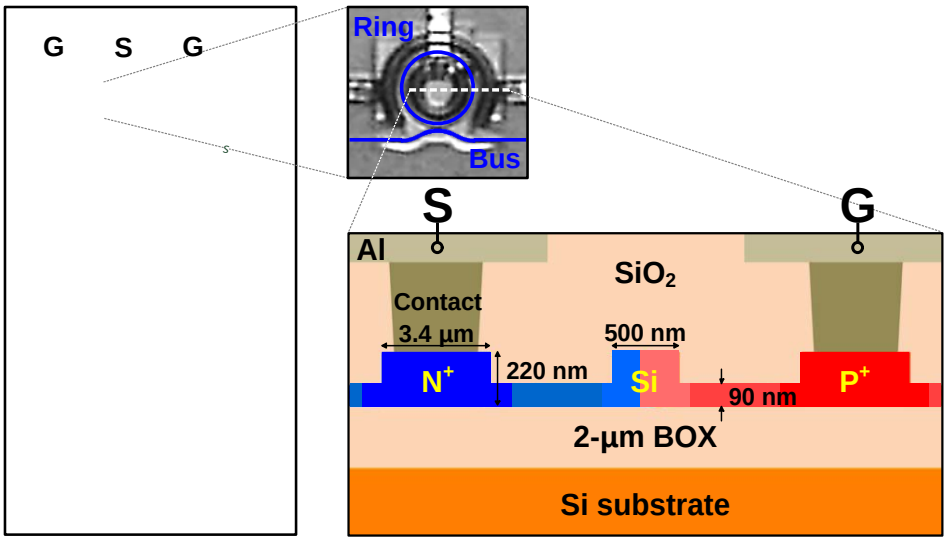

Fig 3-1. Fabricated Si MRM microphotograph and the cross-section structure.

3-2. Experimental Setup

Figure 3-2 shows the experimental setup used for characterizing the fabricated Si MRM. A tunable laser and an optical spectrum analyzer are used for transmission characteristics measurement. A lightwave component analyzer (LCA) is used for measuring Si MRM modulation frequency responses. LCA provides the electrical signals that modulate the Si MRM and detects the modulated output light signals.

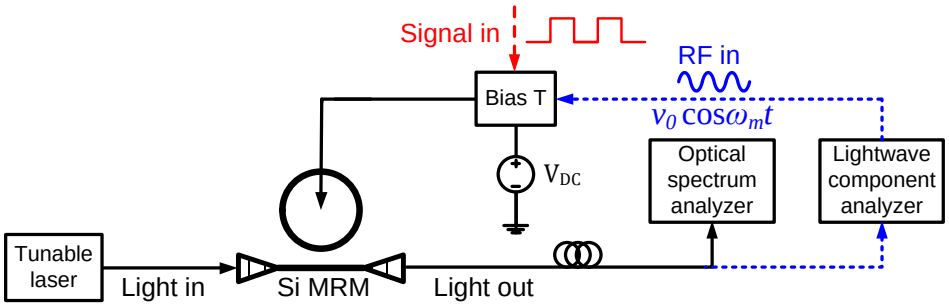

Fig 3-2. Experimentalsetup.

3-3. DC Characteristics

Fig. 3-3 shows DC transmission characteristics of Si MRM depending on input power, 50, 200, 400, 600, and 800 μW. High input power makes skewed transmission curve.

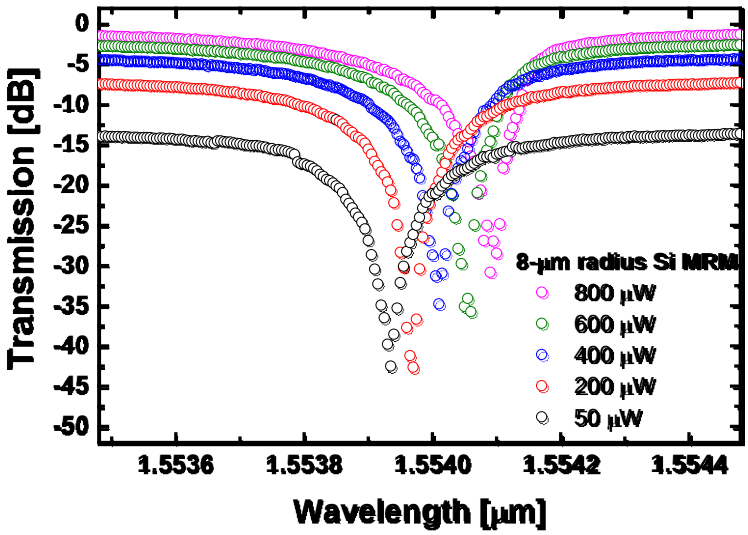

Fig 3-3. DC transmission characteristics depending on input power.

3-4. AC Characteristics

Fig. 3-4 shows AC characteristics of Si MRM depending on detuning. High detuning level makes high AC bandwidth. Also there is optimal detuning point for high modulation efficiency

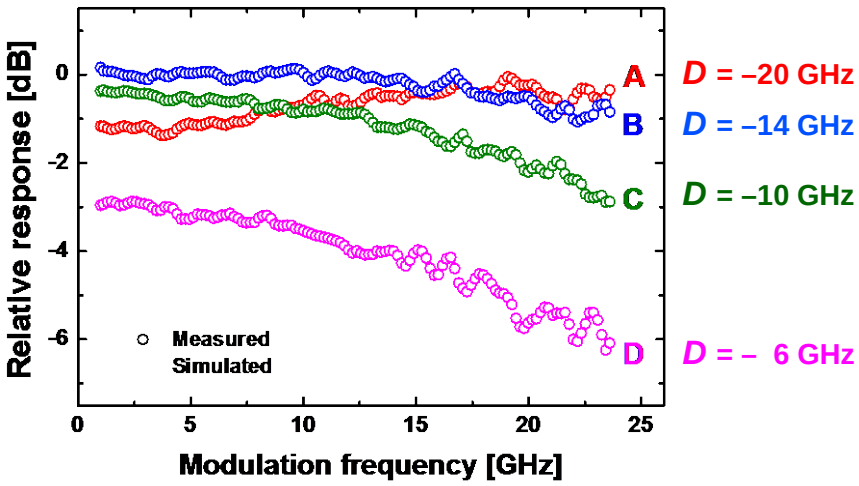

Fig 3-4. AC characteristics depending on detuning.

4. Modeling of Si MRM Dynamics

There have been several reports on Si MRM modulation characteristics analyses using either the time-dependent dynamics model [18] or the coupled-mode theory [19], [20]. Numerical simulations based on these models produce very accurate results but their small-signal approximations [18], [21], [22] can be much easier to use for Si MRM design. Specifically, small-signal approximation given in [18] that is based on the time-dependent dynamics model provides very accurate description of Si MRM modulation characteristics. However, this small-signal model does not provide intuitive understanding of Si MRM modulation dynamics, which can be of great help for design optimization of Si MRMs for target applications. Small-signal models derived from the coupled-mode theory [21] and [22] provide accurate results along with intuitive understanding of modulation dynamics. For example, the model given in [21] provides clear understanding of the peaking behavior of Si MRM frequency response. The model given in [22] is in the form of the second-order system characteristics that can provide straight-forward systematic explanations of Si MRM modulation for both cases of Si MRM refractive index and coupling coefficient modulation. However, in this model, the location for the zero is oversimplified resulting in inaccurate

response when Si MRM is either in the under- or over- coupling condition as will be discussed in this paper.

Most of our small-signal analysis of Si MRM is based on the coupled-mode theory. This model is also in the form of the second-order system characteristics having two complex poles and one real negative zero, but the location of zero is accurately determined. Our model allows an analytical expression for the modulation efficiency at DC modulation frequency, from which the optimal conditions for the best modulation efficiency are determined. The accuracy of our model is experimentally confirmed. Some early results of our investigation have been very briefly reported in [23].

Also, we analyze high-power effect on Si MRM. In [24], it was experimentally demonstrated that Si MRM modulation eye diagram quality changes greatly depending on the modulation data rate. However, there has been no report on Si should be able to simulate the entire Si MRM modulation characteristics reliably. We show that the self-heating effect can be accurately modeled based on the coupled-mode theory and experimentally extract the value of the key physical parameter that determines the dependence of the group refractive index on the injected light power. Furthermore, we implement the model in CADENCE, the most popular CAD tool used for electronic circuit design, so that the modulation characteristics of Si MRMs can be co-simulated with driver electronics.

4-1. Multiple Round-Trip Approach

4-1-1. Large-Signal Model

We assume the phase shift is expressed as, where $v(t)$ is the applied voltage across the junction and $V\pi$ is the voltage required for π phase shift. Using the multiple round-trip approach, output optical field (Eo) at z=0 is given as

$$\begin{aligned} E_o &= \left[\tau - \kappa^2 a \exp\left(-j\theta_1\right) - \kappa^2 a^2 \tau \exp\left(-j\theta_2\right) - \cdots\right] E_i \\ &= \left[\tau - \kappa^2 \sum_{n=1}^{\infty} a^n \tau^{n-1} \exp\left(-j\theta_n\right)\right] E_i \end{aligned} \tag{4.1}$$

where τ and κ are the through and the coupling coefficient, respectively, and α is the round-trip loss of the ring. E_i is the input optical field where η_0 is the effective refractive index of the ring waveguide, and is propagation constant of free space wavelength λ_0. In Eq. (4.1), θ_n is the phase shift experienced by the nth round-trip is given as

$$\exp(-j\theta_n) = \exp\left[-jn\eta_0 k_0 L + j\sum_{k=1}^{n}\int_{z=0}^{z=L} \frac{\pi}{V_\pi} v\left(t - kT + \frac{\eta_0 z}{c}\right) dz\right] \tag{4.2}$$

where L and T represent round-trip length and ring round-trip time, respectively.

5-1-2. Small-Signal Model

$v(t) = v_{DC} + v_0 \cos(\omega_m t)$ is the applied voltage signal where v_{DC} and v_0 are DC bias voltage and AC signal amplitude, respectively, and ω_m is the modulation frequency.

Applying the usual small signal approximation to Eq. (4.1) with $v(t)$, phase shift can be derived as

$$\begin{aligned} -j\theta_n = & -jnL\left(\eta_0 k_0 - \frac{\pi}{V_\pi} v_{DC}\right) \\ & + j\frac{\pi}{V_\pi}\frac{c}{\eta_0}\frac{v_0}{\omega_m}\left[\sin(\omega_m t) - \sin(\omega_m t - n\omega_m T)\right] \end{aligned} \tag{4.3}$$

By substituting Eq. (4.2) into Eq. (4.1), Eq. (4.1) can be expressed as

$$E_o = \left[H_0 + H(\omega_m)\exp(j\omega_m t) + H(-\omega_m)\exp(-j\omega_m t)\right]E_i \tag{4.4}$$

H_0 and $H(\omega_m)$ is given by τ- $\kappa^2 R(0)$ and $\kappa^2 A(\omega)[R(\omega)- R(0)]/2$, respectively, where $A(\omega) = (\pi c v_0)/(V_\pi \eta_0 \omega)$ and $R(\omega) = \left[a\exp(-j(\theta+\omega T))\right]/\left[1-a\tau\exp(-j(\theta+\omega T))\right]$. θ is $\eta_0 k_0 L - \pi L v_{DC}/V_\pi$.

To get the intensity transfer function, we have to derive $E_o(j\omega)/v(j\omega)$ using Fourier transform. Then, the intensity transfer function of the ring modulator for modulation frequency of ω is given as

$$\begin{aligned} T(s) &= H_0^* H(s) + H_0 H(-s)^* \\ &\propto \frac{\kappa^2 c a \tau \sin(\theta)}{V_\pi \eta_0} \frac{\left[\exp(-sT)-1\right]}{s} \\ &\quad \times \frac{a^2\exp(-sT)-1}{a^2\tau^2\exp(-2sT)-2a\tau\exp(-sT)\cos(\theta)+1} \end{aligned} \tag{4.5}$$

5-2. Coupled-Mode Approach

5-2-1. Large-Signal Model

The solution for Eq. (2.11) and Eq. (2.22) with the incident optical field $E_i(t) = E_0 \exp(j\omega t)$ is the sum of the homogeneous and the steady-state solutions, or

$$a(t) = P \exp\left(j\omega_0 t - \frac{1}{\tau} t \right) + Q \exp(j\omega t) \tag{4.6}$$

where P and Q are the homogeneous and steady-state coefficients that need to be determined, respectively. When there is a change in the modulation voltage $v(t)$, it can be approximated with the series of small-step changes having small time interval Δt as

$$v(t) \cong \begin{cases} v_0 = v(t_0), & t_0 \le t < t_1 \\ v_1 = v(t_1), & t_1 \le t < t_2 \\ \vdots & \vdots \\ v_k = v(t_k), & t_k \le t < t_{k+1} \end{cases}. \tag{4.7}$$

Then, corresponding $a(t)$ can be represented as

$$a(t)=\begin{cases} a_0(t)=P_0\exp\left(j\omega_{0,0}t-\dfrac{1}{\tau_0}t\right)+Q_0\exp\left(j\omega t\right), & t_0\le t<t_1 \\ a_1(t)=P_1\exp\left(j\omega_{0,1}t-\dfrac{1}{\tau_1}t\right)+Q_1\exp\left(j\omega t\right), & t_1\le t<t_2 \\ \vdots \qquad\qquad\qquad\qquad\qquad\qquad \vdots & \\ a_k(t)=P_k\exp\left(j\omega_{0,k}t-\dfrac{1}{\tau_k}t\right)+Q_k\exp\left(j\omega t\right), & t_k\le t<t_{k+1} \end{cases} \quad ,(4.8)$$

where P_k and Q_k are the homogeneous and steady-state coefficients, and $\omega_{0,k}$ and τ_k is the ring eparameter values for v_k when $t_k<t\le t_{k+1}$. Since the energy in ring should be continuous at each boundary of time steps, $a_{k-1}(t_k)$ should be equal to $a_k(t_k)$.

Assuming $a(t_0)$ has reached the steady-state, P_0=0 and $a_0(t)=Q_0\exp\left(j\omega t\right)$.

Q_0 can be determined by substituting $a_0(t)=Q_0\exp\left(j\omega t\right)$ into (1) as

$$Q_0=\frac{-j\sqrt{\dfrac{2}{\tau_{e,0}}}}{j\left(\omega-\omega_{0,0}\right)+\dfrac{1}{\tau_0}}E_0 \qquad (4.9)$$

where $\tau_{e,0}$ is the ring parameter values for v_0 when for $t_0<t\le t_1$.

Then,

$$a_1(t_1)=a_0(t_1)=P_0\exp\left(j\omega_{0,0}t_1-\frac{1}{\tau_0}t_1\right)+Q_0\exp\left(j\omega t_1\right). \qquad (4.10)$$

Since $P = \left[a(t) - Q\exp\left(j\omega t \right) \right] \exp\left(-j\omega_0 t + \frac{1}{\tau} t \right)$ from (3), P_1 can be determined as

$$\begin{aligned} P_1 &= \left[a_1(t_1) - Q_1 \exp\left(j\omega t_1 \right) \right] \exp\left(-j\omega_{0,1} t_1 + \frac{1}{\tau_1} t_1 \right) \\ &= \left[a_0(t_1) - Q_1 \exp\left(j\omega t_1 \right) \right] \exp\left(-j\omega_{0,1} t_1 + \frac{1}{\tau_1} t_1 \right). \end{aligned} \tag{4.11}$$

where Q_1 has the same expression as Eq. (4.9) with corresponding $\omega_{0,1}$ $\tau_{e,1}$, and τ_1. Using the boundary condition again, $a_2(t_2) = a_1(t_2)$ and above process can be repeated, or we have following iterative equations:

$$P_k = \left[a_{k-1}(t_k) - Q_k \exp\left(j\omega t_k \right) \right] \exp\left(-j\omega_{0,k} t_k + \frac{1}{\tau_k} t_k \right), \tag{4.12}$$

$$\begin{aligned} a_k(t) &= P_k \exp\left(j\omega_{0,k} t - \frac{1}{\tau_k} t \right) + Q_k \exp\left(j\omega t \right) \\ &= \left[a_{k-1}(t_k) - Q_k \exp\left(j\omega t_k \right) \right] \exp\left(j\omega_{0,k} - \frac{1}{\tau_k} \right)\left(t - t_k \right) + Q_k \exp\left(j\omega t \right) \end{aligned} \tag{4.13}$$

$$\begin{aligned} a_{k+1}(t_{k+1}) &= a_k(t_{k+1}) \\ &= \left[a_{k-1}(t_k) - Q_k \exp\left(j\omega t_k \right) \right] \exp\left(j\omega_{0,k} - \frac{1}{\tau_k} \right) \Delta t + Q_k \exp\left(j\omega t_{k+1} \right). \end{aligned} \tag{4.14}$$

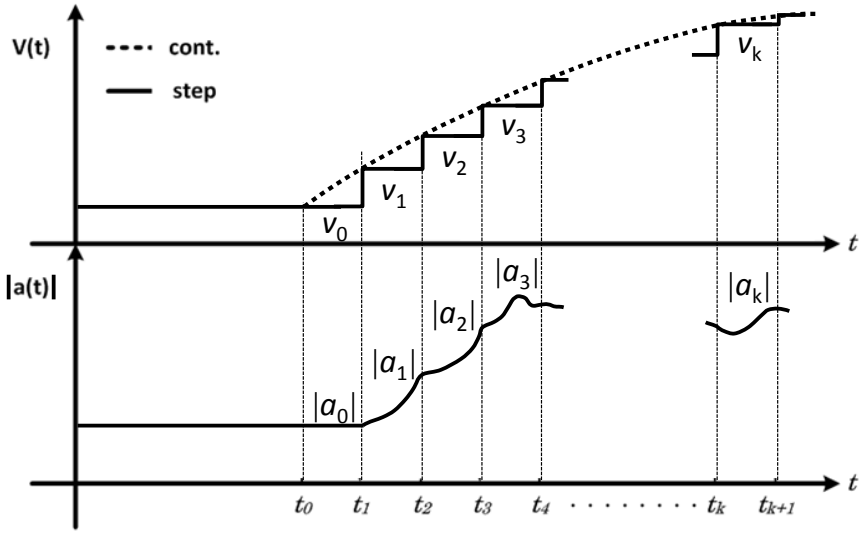

Fig. 4-1. Step change in the modulation voltage and numerical calculation of *a*(t)

5-2-2. Small-Signal Model

When the Si MRM is modulated with a small voltage signal, v = $v_0\cos(\omega_m t)$, having modulation angular frequency ωm around the bias, the change in group index with time, η(t), can be expressed as

$$\eta(t) = \frac{\partial \eta}{\partial v} v_0 \cos(\omega_m t). \tag{4.16}$$

Since both ω0 and 1/τ are proportional to 1/η0, (2.10) can be rewritten as

$$\begin{aligned} \frac{da(t)}{dt} &= \left(j\omega_0 - 1/\tau \right) \frac{\eta_0}{\eta_0 + \eta(t)} a(t) - j\mu E_i(t) \\ &\cong \left(j\omega_0 - 1/\tau \right) \left[1 - \frac{v_0}{\eta_0} \cdot \frac{\partial \eta}{\partial v} \cos(\omega_m t) \right] a(t) - j\mu E_i(t), \end{aligned} \tag{4.17}$$

for η(t)/η0 ≪ 1, which is the case for the small- signal analysis. Since mutual coupling is not much affected by the instantaneous group index change, we assume μ does not change with time. Substituting (4.89) into (2.10) and (2.11), we can express the output light as

$$E_o(t) = E_i(t) - \mu^2 E_0$$
$$\times \exp\left\{ \left(j\omega_0 - 1/\tau \right) \left[t - \frac{v_0 \left(\exp(j\omega_m t) - \exp(-j\omega_m t) \right)}{2 j \omega_m \eta_0} \cdot \frac{\partial \eta}{\partial v} \right] \right\}$$
$$\times \int_{u=0}^{u=t} \exp\left\{ -\left(j\omega_0 - 1/\tau \right) \left[u - \frac{v_0 \left(\exp(j\omega_m u) - \exp(-j\omega_m u) \right)}{2 j \omega_m \eta_0} \cdot \frac{\partial \eta}{\partial v} \right] \right\}$$
$$\times \exp(j\omega u) du. \qquad (4.18)$$

Applying the usual small-signal approximation to (10), we can derive h(t) defined as Eo(t) / Ei(t) as

$$h(t) \cong H_0 + H(\omega_m) \exp(j\omega_m t) + H\left(-\omega_m\right) \exp(-j\omega_m t),$$

where

$$H_0 = \frac{j\omega - j\omega_0 + 1/\tau - \mu^2}{j\omega - j\omega_0 + 1/\tau} \text{ and}$$

$$H(\omega_m) = \mu^2 \frac{v_0}{2 j \omega_m \eta_0} \frac{\partial \eta}{\partial v} \left(\frac{j\omega_0 - 1/\tau}{j\omega - j\omega_0 + 1/\tau} - \frac{j\omega_0 - 1/\tau}{j\omega_m + j\omega - j\omega_0 + 1/\tau} \right). \qquad (4.19)$$

H0 is the Lorentzian-shaped steady-state solution and, H(ωm) and H(–ωm) represent the upper- and lower-side band response, respectively. As expected, H0 shows the resonance characteristic when ω = ω0. For the critical coupling condition (1/τ = μ2), H0 becomes zero at resonance (ω = ω0).

When the modulated optical signal is detected by a photodetector, the generated photocurrent is proportional to light intensity I(t), which can be calculated by |h(t)|2. I(t) contains many terms but we need to consider only

those terms that involve exp(jωmt) since we are interested in the small-signal response to the modulation frequency ωm. This is given as

$$\left[H(\omega_m)H_0^{*}+H^{*}(-\omega_m)H_0\right]\exp(j\omega_m t). \tag{4.20}$$

After taking the Laplace transform of (12), we can obtain Δ(s), the Si MRM small-signal electro-optic modulation response in the s domain, given as

$$\Delta(s)=\frac{I(s)}{V(s)}=\frac{\left|H(s)H_0^{*}+H^{*}(-s)H_0\right|}{v_0/2}. \tag{4.21}$$

If $1/\tau \ll \omega 0$, which is the case for the typical operating wavelength around 1.55 μm, Δ(s) can be re-written in the form of the well-known second-order system having two complex poles and one real zero as

$$\begin{aligned}\Delta(s)&=\frac{\mu^2}{\eta_0}\cdot\frac{\partial\eta}{\partial v}\cdot\frac{2\omega_0 D}{D^2+1/\tau^2}\cdot\frac{s+2/\tau_l}{(s+1/\tau+jD)(s+1/\tau-jD)}\\&=G\cdot\frac{s+2/\tau_l}{s^2+(2/\tau)s+D^2+1/\tau^2},\end{aligned}$$

where $D=\omega-\omega_0$ and

$$G=\frac{\mu^2}{\eta_0}\cdot\frac{\partial\eta}{\partial v}\cdot\frac{2\omega_0 D}{D^2+1/\tau^2}. \tag{4.22}$$

The detuning parameter D represents how much the input light frequency ω is detuned from the ring resonance frequency ω0.

We can rewrite the denominator of the above equation using ωn, the natural angular frequency, and ζ, the damping ratio, as

$$\Delta(s) = G \cdot \frac{s+z}{s^2 + 2\zeta\omega_n s + \omega_n{}^2}, \tag{4.23}$$

where

$$z = 2/\tau_l, \tag{4.24}$$

$$\omega_n = \sqrt{D^2 + 1/\tau^2}, \text{ and} \tag{4.25}$$

$$\zeta = \sqrt{\frac{1/\tau^2}{D^2 + 1/\tau^2}} = \frac{1/\tau}{\omega_n}. \tag{4.26}$$

Figure 4-1 shows the pole-zero diagram corresponding to (14) and (15) for the E-O modulation along with graphical definitions for ωn and ζ. In the figure, the location of zero depends on the MRM coupling condition; $z > 1/\tau$ for under-coupling, $z = 1/\tau$ for critical coupling, and $z < 1/\tau$ for over-coupling.

From the second-order system analysis, it is well known that the damping behavior of a system having two complex poles critically changes at $\zeta = 1$; under-damped for $\zeta < 1$ and over-damped for $\zeta > 1$. As can be seen in (18), Si MRMs have $\zeta < 1$, unless $D = 0$, which is not a desired condition for applications since at this condition modulated output power is very small.

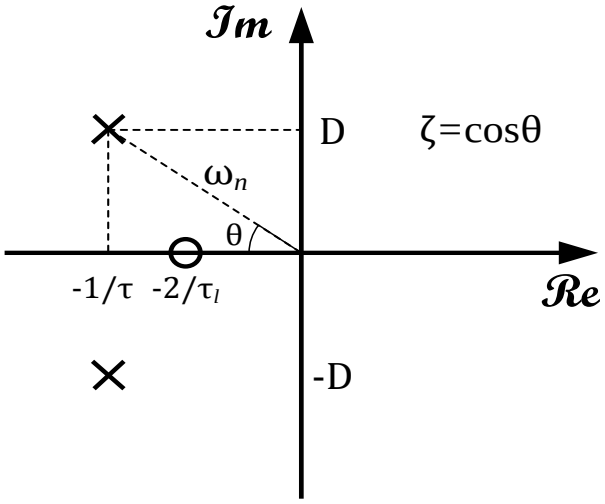

Fig. 4-2. Pole-zero diagram of Si MRM small-signal model

4-3. Self-Heating Effect Implementation

Si MRM is susceptible to the self-heating effect since, with the resonant effect, the injected light can circulate the ring waveguide many times before it escapes. This self-heating effect can be quite significant for Si MRMs based on reverse-biased PN junctions for high-speed modulation since free carriers either in the P- or N-doped ring waveguide can absorb the circulation light.

In PN-junction based Si MRM, the free-carrier absorption (FCA) is the dominant cause for the thermal resonant shift as the heat generated through FCA in the doped ring waveguide increases the group refractive index (Fig. 4-2) [24]. This becomes more pronounced when the input light wavelength is closer to the resonance as the optical power in the ring is higher, resulting in the skewed resonance peak. The group refractive index on k+1th time-step of the ring, η_{k+1}, can be modeled with a function of $|A(t)|^2$, total power flowing through any cross section of the ring waveguide, as

$$\eta_{k+1} = \eta_0 + \Delta\eta_{th} = \eta_0 + \sigma\left|A_k\right|^2 = \eta_0 + \sigma\left|a_k\right|^2 \frac{c}{\eta_k l}, \qquad ()$$

where σ is the coefficient representing the change of group refractive index with optical power.

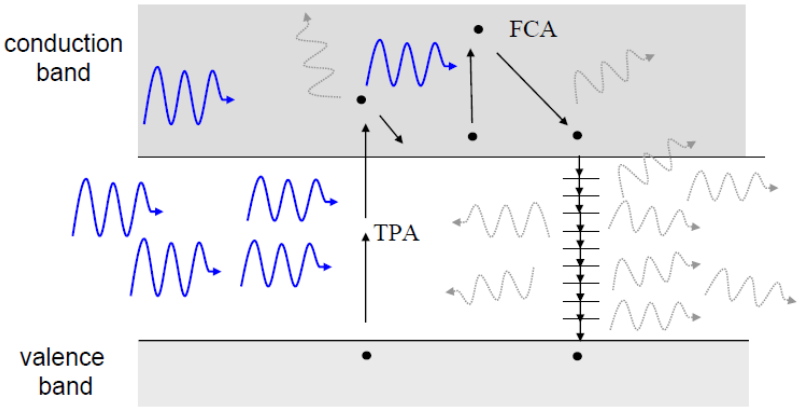

Fig 4-3. Conceptual diagram of self-heating effects

4-4. Discussion

There are several previously reported small-signal modulation models [18], [21], [22]. These can be classified into two types; that based on the time-dependent dynamics model [18] and those on the coupled-mode theory [21], [22]. The former provides very accurate result but it has a somewhat complicated expression, and those in the latter type have more simplified expressions, although the details very from model to model. For accuracy verification, we compare the modulation frequency responses of our model with those produced by small-signal models given in [18] and [22] as these two are the most comprehensive small-signal models reported so far. Comparisons are made in three different conditions as shown in Fig. 3; critical-coupling in Fig. 4-3(a), under-coupling in Fig. 4-3(b), and over-coupling in Fig. 4-3(c).

As can be seen in the Fig. 3(a), all three models produce almost identical results when the ring modulator in the critical-coupling condition. For this calculation, $1/\tau$ = 10-GHz and $2/\tau l$ = 10-GHz are used, which correspond to device parameter values of α= 0.980 and γ = 0.980 γ. However, both in under-coupling condition with $1/\tau$ = 10-GHz and $2/\tau_1$ = 12-GHz, which correspond α= 0.975 and γ = 0.984, and over-coupling with $1/\tau$ = 10-GHz and $2/\tau l$ = 8-GHz, which correspond to device parameter values of α= 0.984 and γ = 0.975,

our model and the model in [18] produce almost identical responses but results from the model given in [22] deviate (Fig. 4- 3(b) and Fig. 4- 3(c)). This is because in [22], z is over-simplified as $1/\tau$, whereas it is given as $1/\tau_1$ more accurately in our model.

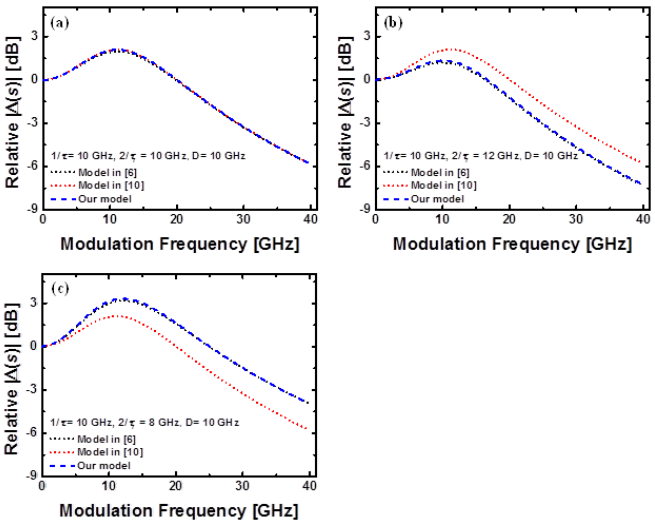

Fig. 4-4. Modulation responses from different models in (a) critical-coupling, (b) under-coupling, and (c) over coupling conditions.

5. Experimental Model Verification

5-1. Parameter Extraction

The first step for experimental verification is extracting numerical values of the model parameters used in our model. This can be done by fitting the measured transmission characteristics with $|H_0|^2$, where H_0 is the steady-state solution of the coupled-mode equation.

5-1-1. Loss and Coupling Coefficients Extraction

Circles in Fig. 5-1 represent the measured transmission characteristics of the Si MRM biased at –1 V. The line shows the calculated $|H_0|^2$ with η_0, $1/\tau$ and $2/\tau_l$ determined by the least mean square method. Table 1 lists the extracted numerical values as well values for α and γ that are determined from the extracted values. To avoid any self-heating effects due to free carrier absorption and two-photon absorption, input optical power lower than –30 dBm was used for the measurement. In addition, the influences of wavelength-dependent transmission characteristics of the grating couplers and electrical frequency responses of the Si MRM are carefully calibrated out.

TABLE II

EXTRACTED PARAMETER VALUES OF SI MRM

Parameter	DESCRIPTION	Value
η_0	Group index (ring waveguide)	3.860659
$1/\tau$	Total decay time constant (GHz)	21.858
$2/\tau_l$	Decay time constant: zero location (GHz)	24.440
α	Round-trip loss coefficient	0.949
γ	Through coefficient (ring-bus coupler)	0.960

5-1-2. Thermal Coefficients Extraction

Eq. (2.1) can be numerically calculated with changing η in each time step using Eq. (2). Figure 2 shows the measured and simulated transmission characteristics at five different power levels (50, 200, 400, 600, and 800 μW) for Si MRMs having three different radii of 6, 10, and 14 μm. Additional coupling loss on measurement is calibrated.

The numerical values for the parameters in the model are obtained by fitting the calculated results to the measured. Specifically, values for η0, 1/τ, and μ2 are extracted from the measurement with the lowest optical power, and σ from the high optical power measurements. The value for σ is around 4×10-5 mW-1 for all different Si MRMs measured. Extracted values for all fitting parameters are demonstrated in Table 2.

TABLE III

Extracted parameter values of Si MRM

Name	Description	Extracted value		
		8-μm radius	10-μm radius	12-μm radius
η_0	Group index	3.864294	3.856766	3.852380
$1/\tau$	Total decay time constant (GHz)	19.73	16.38	14.13
μ^2	Mutual coupling constant (GHz)	19.26	16.19	11.93
σ	Group refractive index change coefficient (mW^{-1})	0.43	0.39	0.38

5-1-3. Electrical Parasitics Extraction

The parameter values for the equivalent-circuit elements are extracted from two-port S-parameter measurements. Advanced Design System (ADS) by Agilent Technology is used for the S-parameter extraction. First, Y-parameters and Z-parameters are calculated from the measured S-parameters(Fig. 5-1) , and open and short test patterns are used for extracting parameters. The extracted parameters are listed in Fig. 5-2. Then, other parameters are extracted through a fitting process. The frequency-dependent current source is not included during this extraction and fitting process since it does not influence the values of passive circuit elements in the small-signal analysis. For fitting, initial guesses are made from theoretical equations and then manually.

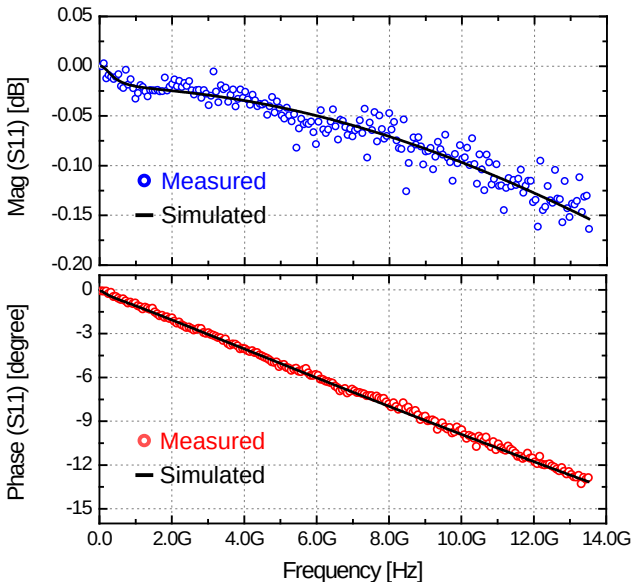

Fig. 5-1. Extracted electrical parasitics.

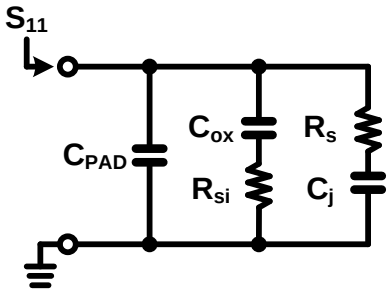

Parameters

C_{PAD}	C_j	C_{ox}	R_s	R_{si}
13.4 fF	14.7 fF	21.3 fF	211	19.3 k

Fig. 5-2. Extracted electrical parasitics values.

5-2. Model Verification

5-2-1. Small-Signal Models

Figure 7 shows the measured modulation frequency responses of the Si MRM at four different D values of –20 GHz (A), –14 GHz (B), –10 GHz (C), and –6 GHz (D), whose locations are shown in the inset of Fig. 6, as well as the calculated responses of our small-signal model with the extracted parameter values given in Table 1.

To avoid any self-heating effects due to free carrier absorption and two-photon absorption, input optical power lower than –30 dBm was used for the measurement. In addition, the influences of wavelength-dependent transmission characteristics of the grating couplers and electrical frequency responses of the Si MRM are carefully calibrated out.

In Fig. 7, the measured and calculated results are normalized to the low-frequency value of the case (B). Differences in low-frequency responses for different D values are due to the difference in G given in (14). The largest bandwidth is achieved for D = –20 GHz (A) with the largest ω_n and the smallest ζ. As can be seen in the figure, measurement and calculated results are in very good agreement confirming the accuracy of our small-signal model.

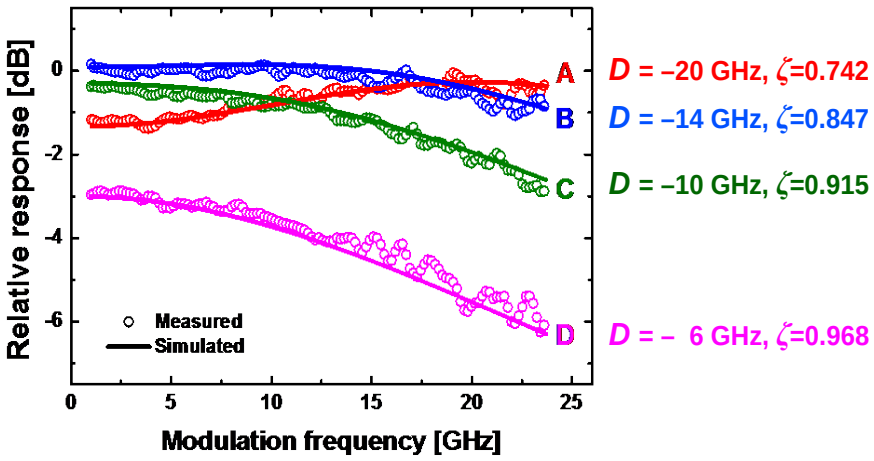

Fig. 5-3. Measured relative frequency responses at different detuning levels

6. Consideration about Optimal Conditions for Si MRM

6-1. Si MRM Analysis Using Small-Signal Model

To optimize Si MRM design for desired optical transmitter performance, such transient behaviors as rising and falling overshoots and ripples should be carefully considered as well as the modulation efficiency and bandwidth. Although our small-signal model cannot provide large-signal transient characteristics, it allows an intuitive interpretation of transient characteristics. Figure 9(a) shows the normalized transient responses of the Si MRM having $1/\tau$ = 9.7364 GHz, D = –15.2173 GHz, and ζ = 0.5389 for the on-state and $1/\tau$ = 9.7367 GHz, D = –8.7826 GHz, and ζ = 0.7426 for the off state. This transient response is obtained by numerically solving the coupled-mode equations given in (1) and (2). A time step smaller than round-trip time c/(n0L) of the ring is used to make sure that the simulation results correctly reflect the ring resonator dynamics. For the simulation, the Si MRM bias voltage abruptly changes from 0 to –2 and then back to 0 V. Changes in group index with above voltage changes is determined by simulation with Synopsys Sentaurus Device and Lumerical Mode Solutions using the Si MRM fabrication parameters provided by OpSIS-IME.

As can be seen in the Fig. 9(a), the rising edge has a different amount of overshoot from the falling edge. This can be easily explained using our small-signal model with different parameter values for the rising and falling edges. For the rising edge, parameter values of the Si MRM biased at –2 V can be used, and for the falling edge, biased at 0 V. Figure 9(b) and 9(c) show the small-signal step responses along with the transient responses of the large-signal numerical solution for the rising and the falling edges, respectively. They are in good agreement allowing us to use such small-signal model parameters as D and $1/\tau$ for overshoot and undershoot behavior interpretation as shown in the figure. In short, the overshoot amount is decided by ζ and z, the envelope of the response exponentially decays with time constant τ, the oscillation frequency is |D|.

6-1-1. Modulation Efficiency

From (14), the DC gain of $\Delta(s)$, or the modulation efficiency can be obtained as

$$\left|\Delta(s=0)\right| = \frac{2}{\eta_0}\cdot\frac{\partial\eta}{\partial v}\cdot\frac{\omega_0\left|D\right|(2/\tau - z)\,\mathrm{z}}{(1/\tau^2 + D^2)^2}. \qquad (6.1)$$

With this, we can determine the optimal condition that provide the largest modulation efficiency by finding the point where $\partial\Delta(s=0)/\partial z = 0$. Since

$$\frac{\partial\Delta(s=0)}{\partial z}=\frac{4}{\eta_0}\cdot\frac{\partial\eta}{\partial v}\cdot\frac{\omega_0|D|(1/\tau-z)}{(1/\tau^2+D^2)^2}, \tag{6.2}$$

$z = 1/\tau$ satisfies the required condition. From (4) and (17), this corresponds to, or the critical coupling condition.

We can further determine the value of D that provides the largest modulation efficiency by finding the condition for $\partial\Delta(s=0)/\partial D=0$. From (14),

$$\frac{\partial\Delta(s=0)}{\partial D}=\frac{2\mu^2\omega_0 z}{\eta_0}\cdot\frac{\partial\eta}{\partial v}\cdot\frac{(1/\tau^2-3D^2)}{(D^2+1/\tau^2)^3}, \tag{6.3}$$

which becomes zero when $D = 1/(\sqrt{3}\cdot\tau)$. The ratio of transmitted to the input optical intensity when the input wavelength satisfies this condition can be determined from (13) as

$$\left|H_{0,opt}\right|^2=\left|\frac{j/\sqrt{3}\tau+1/\tau-\mu^2}{j/\sqrt{3}\tau+1/\tau}\right|^2=\frac{1/\tau^2+3/{\tau_e}^2-3/(\tau\cdot\tau_e)}{1/\tau^2}. \tag{6.4}$$

When the Si MRM satisfies the critical coupling condition with , (22) simply becomes 0.25. This tells us that the largest modulation efficiency can

be achieved when the Si MRM is in critical-coupling condition and the input wavelength produces 25% transmission. This result agrees with the experimental observation that the largest modulation efficiency is achieved at the wavelength which has around –6 dB bias loss with respect to the maximum transmission [16]. Even when the coupling condition of the Si MRM has small shift from the critical coupling condition, evaluation of (22) produces values that are not much different from 0.25.

6-1-2. Modulation Frequency Response

Figure 8(a) shows the calculated transmission characteristics for Si MRMs having three different critical coupling conditions ($1/\tau$ = 9.74, 12.14, and 14.53 GHz). Since $1/\tau$ is inversely proportional to the quality factor Q, a MRM with smaller $1/\tau$ has larger Q or shaper transmission characteristics. Figure 8(b), 8(c), and 8(d) show the frequency responses for different critical coupling conditions at three different detuning values, D = –1 MHz for Fig. 8(b), D = –6 GHz for Fig. 8(c) and D = –12 GHz for Fig. 8(d). The amount of detuning is indicated for each case by dotted lines in Fig. 8(a). Only negative detuning values are considered here because the frequency response depends on D2, as can be seen in (16) and (17). As Fig. 8(b), 8(c), and 8(d) show, the amount of detuning greatly influences the frequency response. For D = –1 MHz, the 3-dB bandwidth is less than 20 GHz (Fig. 8(b)), but it is larger than 30 GHz for D = –12 GHz (Fig. 8(d)). This is because larger |D| produces larger ωn and smaller ζ according to (16) and (17). Pronounced peaking is observed in Fig. 8(d) due to small ζ. In several previously published reports (for example, in [17]), it has been claimed that larger quality factor Q decreases Si MRM modulation bandwidth. This is not true for the case of the strongly under-damped MRM as can be seen in Fig. 8(d) where the modulator with the largest Q has the largest 3-dB bandwidth. This is because in this case the MRM with larger Q has a

large amount of frequency peaking due to smaller ζ. This clearly demonstrates that detuning value as well as Q should be carefully considered in order to achieve the desired frequency response of the Si MRM. For such consideration, our small-signal model given in (15) with the well-known second-order system characteristics is very convenient to use.

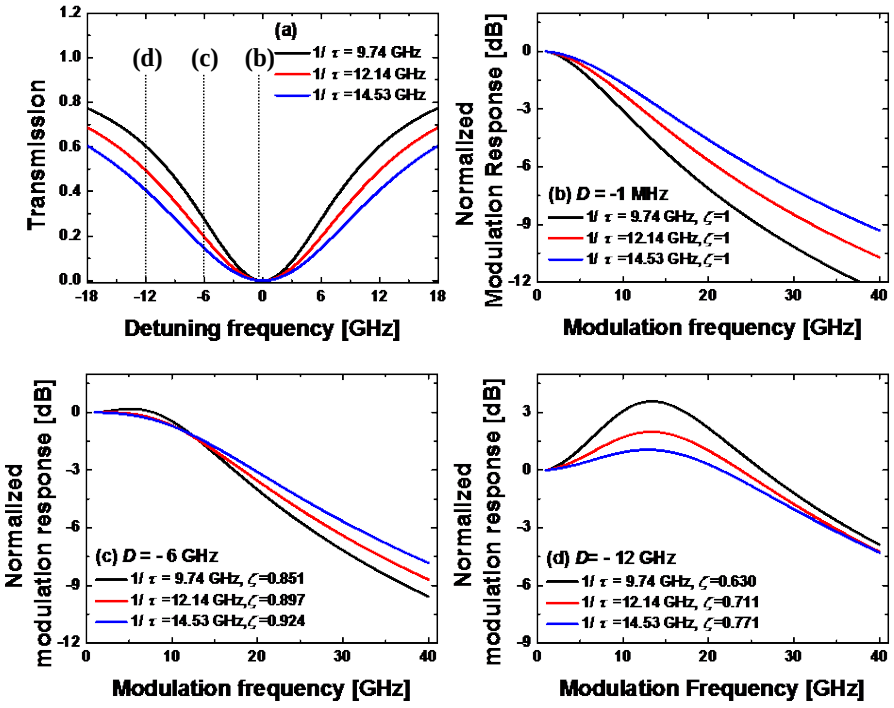

Fig. 6-1. (a) Transmission characteristics with different α and γ values. Normalized Δ(s) with different ωn and ζ values for (b) D = –1 MHz, (c) D = –6 GHz, and (d) D = –12 GHz.

6-2. Si MRM Power Dependence: Self-Heating Effects

We implemented the behavior model for Si MRM dynamics including the self-heating effect in CADENCE, the most popular CAD tool used for electronic circuit design, with Verilog-A. The thermal dissipation time constant for Si is set at 1 μs. Figure 6-2 shows eye diagrams of the Si MRM modulated by 1 Gbps PRBS7 driving signals at three different input power levels of 250 μW, 500 μW, and 750 μW for three different operating wavelengths. As can be seen, the modulation characteristics depend greatly on optical powers as well as the input light wavelengths. This is because the average modulated optical power heats up the Si MRM, resulting in the group refractive index and the shift of Si MRM transfer characteristics. This clearly demonstrates that the light power as well as the wavelength is a critical parameter that needs to be carefully controlled in order to optimize Si MRM modulation characteristics. With our Si MRM self-heating model, the influence of self-heating can be accurately described.

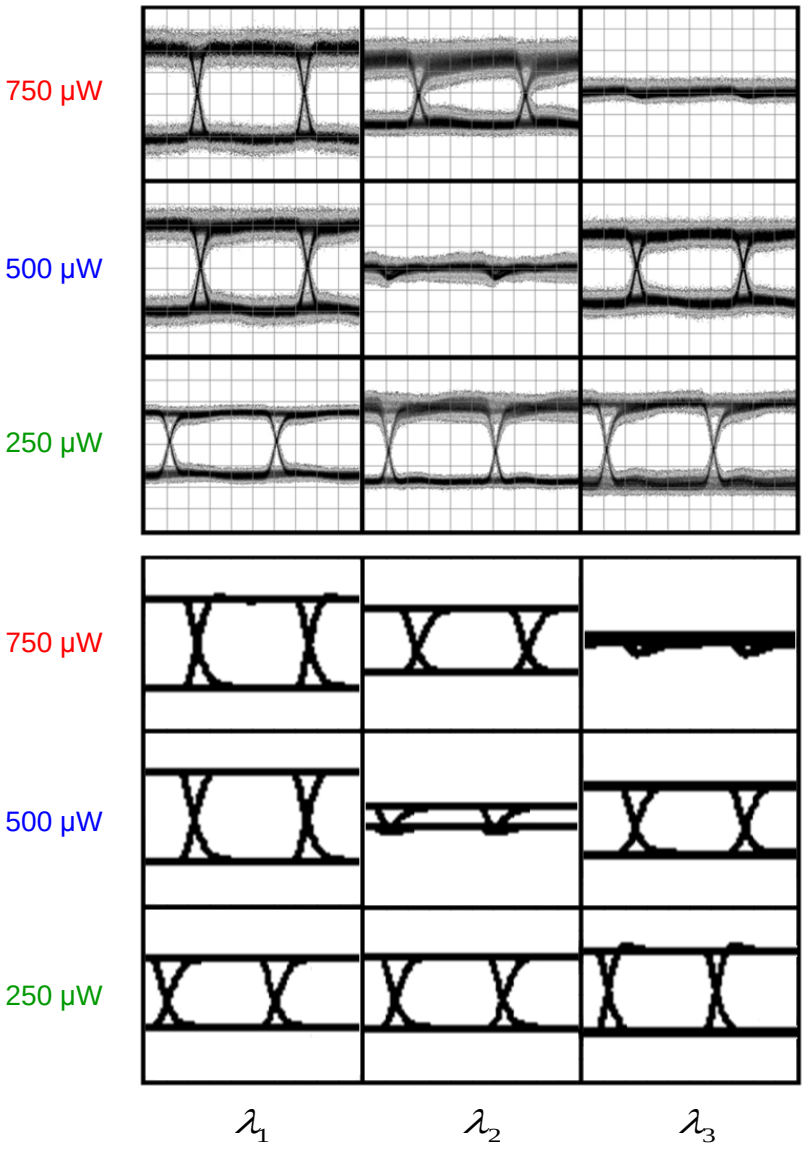

Fig. 6-2. Measured and simulated normalized eye diagrams at different wavelength with different input power levers.

7. Summary

In this thesis, we presented a full modulation model of the Si MRM based on the coupled mode theory. The accuracy of our model is confirmed with experimental measurement. Our model is in the form of the well-known second order system with two complex poles and one real negative zero. With this, it allows determination of the best modulation efficiency condition and easy interpretation of how the frequency and transient responses of the Si MRM depend on various device parameters. The model should be very helpful for designing and analyzing Si MRM device structure that can provide the optimal performance for the target application.

REFERENCES

[1] A. Alduino and M. Paniccia, “Interconnects: Wiring electronics with light,”, Nature Photonics, vol. 1, 153 - 155 (2007).

[2] K. Bergman, L. P. Carloni, A. Biberman, J. Chan, and G. Hendry, "Photonic Network-onChip Design," Springer (2014)

[3] R. Soref, “The past, present, and future of silicon photonics,” IEEE J. Sel. Top. Quantum Electron., vol. 12, no. 6, pp. 1678-1687, 2006.

[4] Q. Xu, B. Schmidt, S. Pradhan, and M. Lipson, “Micrometre-scale silicon electro-optic modulator,” Nature vol. 435, pp. 325-327, 2005

[5] J. F. Buckwalter, et al, IEEE J. Solid-State Circuits, vol.47, no.6, pp.1309–1322 (2012).

[6] L. Zimmermann, et al, European Conference on Optical Communication (ECOC) (2013).

[7] P. Dong, S. Liao, D. Feng, H. Liang, D. Zheng, R. Shafiiha, C.-C. Kung, W. Qian, G. Li, X. Zheng, A. V. Krishnamoorthy, and M. Asghari, “Low Vpp, ultralow-energy, compact, high-speed silicon electro-optic modulator,” Opt. Express, vol. 17, no. 25, pp. 22484-22490, 2009.

[8] G. Li, A.V. Krishnamoorthy, I. Shubin, J. Yao, Y. Luo, H. Thacker, X. Zheng, K. Raj, and J.E. Cunningham, “Ring resonator modulators in silicon for

interchip photonic links," IEEE J. Sel. Top. Quantum Electron., vol. 19, pp. 3401819, 2013.

[9] X. Li, H. Xu, Y. Hu, K. Xiong, Z. Li, T. Chu, J. Yu, and Y. Yu, "44-Gb/s silicon microring modulators based on zigzag PN junctions," IEEE Photonics Technol. Lett., vol. 24, no. 19, pp. 1712-1714, 2012.

[10] R. Soref and B. Bennett, "Electrooptical effects in silicon", IEEE J. Quantum Electron., vol. 23, no. 1, pp. 123-129, 1987.

[11] K.-P. Ho and J. M. Kahn, "Optical frequency comb generator using phase modulation in amplified circulating loop," IEEE Photon. Technol. Lett., vol. 5, no. 6, pp. 721–725, Jun. 1993.

[12] W. Bogaerts, P. D. Heyn, T. V. Vaerenbergh, K. D. Vos, S. K. Selvaraja, T. Claes, P. Dumon, P. Bienstman, D. V. Thourhout, and R. Baets, " Silicon microring resonators,"

[13] H. A. Haus, "Coupling of modes -resonators and couplers," in Waves and fields in optoelectronics, Prentic-Hall, Inc. Englewood Cliffs New Jersey 07632, 1984.

[14] B. E. Little, S. T. Chu, H. A. Haus, J. S. Foresi, and J.-P. Laine, "Microring resonator channel dropping filter," J. Lightwave Technol., vol. 15, pp. 998-1005, 1997.

[15] Reed, G. T. & Knights, A. P. Silicon Photonics: An Introduction Ch. 4, 97–103 (Wiley, 2004).

[16] Cocorullo, G. & Rendina, I. Thermo-optical modulation at 1.5 μm in silicon etalon. Electron. Lett. 28, 83–85 (1992).

[17] M. Nedeljkovic, R. Soref, and G.Z. Mashanovich. \Free-Carrier Electrorefraction and Electroabsorption Modulation Predictions for Silicon Over the 1-14 micron In-frared Wavelength Range". Photonics Journal, IEEE 3.6 (2011), pp. 1171 {1180. issn: 1943-0655. doi: 10.1109/JPHOT.2011.2171930 (cit. on pp. 112, 113).

[18] W. D. Sacher and J. K. S. Poon, “Dynamics of microroing resonator modulators,” Opt. Express, vol. 16, no. 20, pp. 15741-15753, 2008.

[19] L. Zhang, Y. Li, J.-Y. Yang, M. Song, R. G. Beausoleil, and A. E. Willner, “Silicon-based microring resonator modulators for intensity modulation,” IEEE J. Sel. Top. Quantum Electron., vol. 16, no. 1, pp. 149-158, 2010.

[20] M. Song, L. Zhang, R. G. Beausoleil, and A. E. Willner, “Nonlinear distortion in a silicon microring-based electro-optic modulator for analog optical links,” IEEE J. Sel. Top. Quantum Electron., vol. 16, no. 1, pp. 185-191, 2010.

[21] J. Müller, F. Merget, S. Sharif Azadeh, J. Hauck, S. Romero García, B. Shen and J. Witzens, “Optical Peaking Enhancement in High-Speed Ring Modulators,” Scientific Reports, vol. 4, no. 6310, pp. 1-9, 2014.

[22] B. Pile and G. Taylor, “Small-signal analysis of microring resonator modulators,” Opt. Express, vol. 22, no. 12, pp. 14913-14928, 2014.

[23] Y. Ban, J.-M. Lee, B.-M. Yu, S.-H. Cho, and W.-Y. Choi, “Small-signal frequency responses for Si micro-ring modulator,” IEEE Optical Interconnects Conf., pp. 47-48, 2014.

[24] X. Zheng, Y. Luo, G. Li, I. Shubin, H. Thacker, J. Yao, K. Raj, J. E. Cunningham, and A. V. Krishnamoorthy, “Enhanced optical bistability from self-heating due to free carrier absorption in substrate removed silicon ring modulators,” Opt. Express 20(10), 11478-11486 (2012).

국 문 요 약

실리콘 기반 마이크로-링 모듈레이터의 모델링

본 연구에서는 실리콘 마이크로-링 모듈레이터의 모델을 구현하였다. 실리콘 마이크로-링 모듈레이터를 이용하면 높은 주파수의 모듈레이션 대역폭 동시에 적은 에너지로 Cost-effective 하게 광 소자와 전기회로를 동작시킬 수 있다.

본 연구에서 제안하는 모델은 익히 알려진 Coupled-mode theory 를 기반으로 도출되었으며, 두 개의 complex pole 과 하나의 real negative zero 를 가진 잘 알려진 second-order 시스템 특성을 가진다. 성공적인 EPIC 구현을 위해, 전기회로를 디자인 할 때 한 플렛폼에서 광소자와 함께 co-simulate 하여야 한다. 본 연구에서는 이러한 간단하고 사용하기 쉬운 behavior model 을 Verilog-A 기반으로 구현하였다.

이 모델은 아주 정확하게 실리콘 마이크로-링 모듈레이터의 모듈레이션 특성을 설명할 수 있으며, pole-zero diagram 을 통해 직관적인 분석을 가능하게 한다. 모델의 정확성은 기존에 발표되어진 여러 모델들과 비교되었을 뿐만 아니라, 측정 결과와도 비교되었다. 이 모델을 사용함으로써, 가장 효율적인 디자인 파라미터들과 동작점을 얻어 낼 수 있으며, large-signal 데이터 전송에서의 특성도 예측할 수 있다. 모델을 검증하기 위해 DC transmission 특성과, AC 특성, 그리고 Eye-diagram 의 측정하였고, 본 모델을 사용한 시뮬레이션 결과들이 이러한 측정결과와 잘 맞음을 확인하였다.

핵심어 : Coupled mode 분석, 광 모듈레이션, 마이크로-링 모듈레이터, 실리콘 포토닉스